Symmetry and Models of Single-Wall BN and TiO_2 Nanotubes with Hexagonal Morphology

R. A. Evarestov,*,† Yu. F. Zhukovskii,‡ A. V. Bandura,† and S. Piskunov‡,§,∥

Department of Quantum Chemistry, St. Petersburg State University, 26 Universitetsky Avenue, Petrodvorets 198504, Russia, Institute of Solid State Physics, University of Latvia, 8 Kengaraga Str., Riga LV-1063 Latvia, Faculty of Computing, University of Latvia, 19 Raina Blvd., Riga LV-1586, Latvia, and Faculty of Physics and Mathematics, University of Latvia, 8 Zellu Str., Riga LV-1002, Latvia

Received: July 25, 2010; Revised Manuscript Received: October 23, 2010

For ab initio simulations on hexagonal single-wall BN and TiO_2 nanotubes (SW NTs), we have applied the formalism of line symmetry groups describing one-periodic (1D) nanostructures with rotohelical symmetry. Both types of NTs can be formed by rolling up the stoichiometric nanosheets of either (i) a (0001) monolayer of BN hexagonal phase or (ii) a three-layer (111) slab of fluorite-type TiO_2 phase. Optimized parameters of the atomic and electronic structure of corresponding slabs and nanotubes have been calculated using hybrid LCAO method as implemented in CRYSTAL code. Their band gaps ($\Delta\varepsilon_{gap}$) and strain energies (E_{strain}) have been analyzed as functions of NT diameter (D_{NT}). For hexagonal BN and TiO_2 nanotubes, certain qualitative similarities between the $\Delta\varepsilon_{gap}(D_{NT})$ or $E_{strain}(D_{NT})$ functions exist despite the different chemical nature.

1. Introduction

Boron nitride and titania are well-known semiconductors comprehensively studied in materials science, thanks to their widespread technological applications. Six polymorphs of BN have been established so far (including amorphous structure),[1] the most stable among them being cubic and hexagonal phases. The number of discovered TiO_2 polymorphs is seven,[2] although rutile and anatase undoubtedly prevail because of their higher stability as compared to other titania phases. Nanotubes (NTs) of different morphology from these substances were systematically synthesized during the last 10−15 years and carefully studied as prospective technological materials, both for BN[3–7] and TiO_2.[8–11] One recently discovered nanotube application was doping of TiO_2 NTs by boron and nitrogen atoms[12] gradually varied their band gaps.

Since the growth mechanism for both BN and TiO_2 nanotubes is still not well-defined, their comprehensive theoretical studies attract enhanced attention. Numerous simulations were performed so far on 1D single-wall (SW) and multi-wall (MW) models of BN nanotubes possessing hexagonal honeycomb morphology and the two equilibrium structures with either armchair (*ac*) or zigzag (*zz*) type chirality and a wide range of uniform diameters (0.5−2 nm).[13–17] In most theoretical simulations on titania nanotubes, a model 3D → 2D → 1D of structural transformations described in ref 18 was applied, i.e., the bulk (3D) phase first formed a lamellar product (3D → 2D) and then was bent and rolled to a nanotubular form (2D → 1D). The lamellar product was mainly formed by an anatase (101) surface, identified as prevailing in TiO_2 NTs.[19–24] Further geometry optimization of a three-layer O−Ti−O sheet for 2D → 1D transition results in formation of titania nanotubes possessed hexagonal fluorite-like (111) morphology with (*n*,*n*) and (*n*,0) chiralities.[24] This hexagonal structure can really exist in a metastable phase of bulk titania under extremely high pressure.[2]

In this study, we perform comparative descriptions for hexagonal SW nanotubes for BN[17] and TiO_2[24] begun previously. In section 2, we consider the line group symmetry for these nanotubes. A new approach to the generation of the line group irreducible representations is suggested based on the isomorphism between line and plane groups. The application of the approach suggested to nanotubes is demonstrated for X-point of 1D Brilloin zone and line group families 4 and 8. Section 3 describes computational details used for calculations on nanosheets and nanotubes. In sections 4 and 5, we analyze the results calculated for SW hexagonal BN and TiO_2 models, respectively, systematize, and discuss them. Section 6 summarizes the main conclusions.

2. Symmetry of SW BN and TiO_2 Hexagonal Nanotubes

2.1. Layer Folding in the Nanotube Construction. The nanotube symmetry and structure can be simply described using the so-called layer folding which means the construction of the cylindrical surfaces of nanotubes by rolling up the two-periodic (2D) crystalline layers (sheets and slabs). In the case of BN the folding procedure is applied to a graphene-like (0001) nanosheet cut from the most stable phase of bulk crystal with the hexagonal space group 194 ($P6_3/mmc$). The sheet symmetry is described by layer group 78 ($P\bar{6}m2$); see Table 1. For comparison the layer group of a graphene (0001) nanosheet is also given. In both cases all the rolled sheet atoms are distributed over the NT cylindrical surface.

Let **a** and **b** be the primitive translation vectors of the two-periodic (2D) lattice of the layer and γ- the angle between them. To specify the symmetry of nanotubes as monoperiodic (1D) systems, it is necessary to define a finite 1D translation vector $\mathbf{L} = l_1\mathbf{a} + l_2\mathbf{b}$ along the nanotube axis and normal to the chiral vector $\mathbf{R} = n_1\mathbf{a} + n_2\mathbf{b}$, ($l_1$, l_2, n_1, and n_2 are integers). The nanotube of the chirality (n_1, n_2) is obtained by folding the layer in a way that the chiral vector **R** becomes the circumference of the nanotube.

The orthogonal vectors **R** and **L** are connected with the 2D lattice translation vectors **a** and **b** by the transformation

* To whom correspondence should be addressed, re1973@re1973.spb.edu.
† Department of Quantum Chemistry, St. Petersburg State University.
‡ Institute of Solid State Physics, University of Latvia.
§ Faculty of Computing, University of Latvia.
∥ Faculty of Physics and Mathematics, University of Latvia.

10.1021/jp106929f
Published on Web 11/19/2010

TABLE 1: Line Symmetry Groups of SW BN and TiO_2 Nanotubes Rolled up from Hexagonal Nanosheets[a]

object	space group for C, BN, and TiO_2 bulk	layer	layer group	line groups for special chiralities[b]	P_i	line groups for general chiralities (n_1,n_2)
graphene	194	(0001)	80 ($P6/mmm$)	13i	D_{2nh}	5 n_q22 (D_p)
monolayer	$P6_3/mmc$			$(2n)_n/mcm$		
BN	194	(0001)	78 ($P\bar{6}m2$)	4h $(2n)_n/m$	C_{2nh}	1 n_q (C_p)
monolayer	$P6_3/mmc$			8g $(2n)_nmc$	C_{2nv}	
3-layer TiO_2	225	(111)	72 ($P\bar{3}m1$)	4h $(2n)_n/m$	C_{2nh}	1 n_q (C_p)
slab (fluorite)	$Fm\bar{3}m$			8g $(2n)_nmc$	C_{2nv}	

[a] For comparison, the layer group of graphene is added. [b] Special chiralities: g: $(n,0)$, $(0,n)$, $(-n,n)$; h: (n,n), $(-n,2n)$, $(-2n,n)$; i: $(n,0)$, $(0,n)$, $(-n,n)$, (n,n), $(-n,2n)$, $(-2n,n)$.

$$\begin{pmatrix}\mathbf{R}\\ \mathbf{L}\end{pmatrix} = \mathbf{Q}\begin{pmatrix}\mathbf{a}\\ \mathbf{b}\end{pmatrix}$$

The determinant

$$q = \begin{vmatrix} n_1 & n_2 \\ l_1 & l_2 \end{vmatrix}$$

of the matrix

$$\mathbf{Q} = \begin{pmatrix} n_1 & n_2 \\ l_1 & l_2 \end{pmatrix}$$

is equal to the number of 2D lattice points in the 2D supercell formed by the chiral **R** and translation **L** vectors.

The orthogonality relation $(\mathbf{RL}) = 0$ can be written in the form

$$\frac{l_1}{l_2} = -\frac{n_2a^2 + n_1ab\cos\gamma}{n_1b^2 + n_2ab\cos\gamma} \qquad (1)$$

where $a = |\mathbf{a}|$ and $b = |\mathbf{b}|$.

If n is the largest common devisor of n_1 and n_2 ($\tilde{n}_1 = n_1/n$, $\tilde{n}_2 = n_2/n$), one can introduce the reduced translation vector $\tilde{\mathbf{R}}$ along the direction of the vector **R**

$$\tilde{\mathbf{R}} = \frac{1}{n}\mathbf{R}; \quad \begin{pmatrix}\tilde{\mathbf{R}}\\ \mathbf{L}\end{pmatrix} = \tilde{\mathbf{Q}}\begin{pmatrix}\mathbf{a}\\ \mathbf{b}\end{pmatrix}; \qquad (2)$$

$$\tilde{\mathbf{Q}} = \begin{pmatrix} \tilde{n}_1 & \tilde{n}_2 \\ l_1 & l_2 \end{pmatrix}; \quad \tilde{q} = \det(\tilde{\mathbf{Q}}) = \frac{q}{n}$$

Nanotubes, being monoperiodic systems, have a line group symmetry $L = ZP$,[25,26] where P is the point factor and Z is the generalized translation group. The point factor P is a subgroup of an axial point group P_i belonging to one of the point symmetry groups leaving the nanotube axis invariant (C_n, S_{2n}, C_{nv}, C_{nh}, D_n, D_{nd}, D_{nh}). The line group can be factorized also as $L = TP_i$ where T is the subgroup of the pure translations along the nanotube axis. Such a factorization is traditional in crystallography and it is accepted for the monoperiodic rod groups[27] being a particular case of line groups for $n = 1, 2, 3, 4, 6$. The group Z is infinite and cyclic, describing either the glide plane reflections

$$T' = \left(\sigma_v\middle|\frac{1}{2}\right)$$

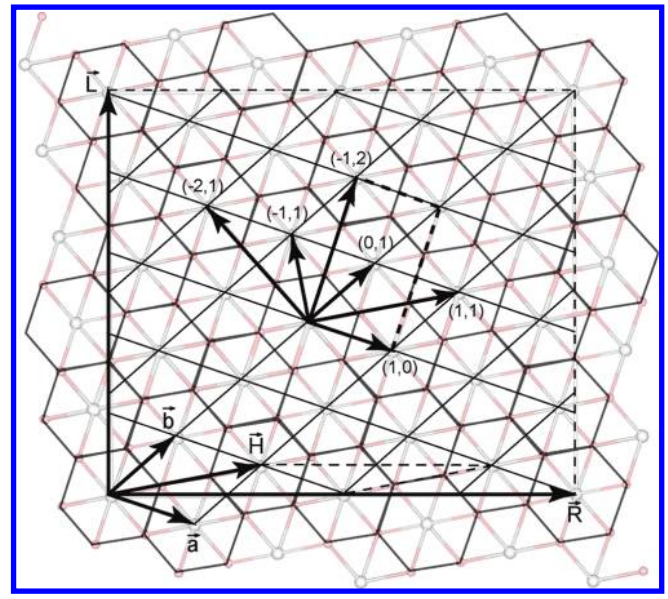

Figure 1. Chiral **R** (4,2), translation **L** (−4,5), helical **H** (1,1) and special chirality vectors for hexagonal lattice.

or the screw axis rotations by $2\pi/n\tilde{q}$ (for $\tilde{q} > 1$) generated by helical operations

$$T_q^{\,r} = \left(C_q^{\,r}\middle|\frac{1}{\tilde{q}}\right)$$

where r is an integer. For $n > 1$, pure rotations appear and form subgroups of point symmetry group P.

The smallest helical vector **H** is defined as

$$\mathbf{H} = h_1\mathbf{a} + h_2\mathbf{b} = \frac{r}{q}\mathbf{R} + \frac{1}{\tilde{q}}\mathbf{L}$$

and satisfies the following conditions: $\tilde{n}_1h_2 - \tilde{n}_2h_1 = 1$; $h_1l_2 - h_2l_1 = r$. The projections of the helical vector **H** on the chiral vector **R** and translation vector **L** define the rotational and translational parts of helical rotation $T_q^{\,r}$, respectively. Figure 1 shows **R** (4,2), **L** (−4,5) and **H** (1,1) vectors for hexagonal lattice.

The symmetry of a nanotube is defined by (i) nanotube chirality (n_1,n_2), (ii) translation vector components (l_1,l_2) found from the orthogonality relation, eq 1, (iii) point symmetry of the rolled 2D lattice (see below). The orthogonality relation has different forms for different 2D lattices. For the hexagonal lattices ($\cos\gamma = 0.5$; $a = b$) relation 1 is transformed to

$$\frac{l_1}{l_2} = -\frac{2n_2 + n_1}{2n_1 + n_2} \tag{3}$$

It is well seen from eq 3 that the nanotube translational symmetry may exist for any chirality (n_1,n_2) if the nanotube is obtained by folding the layer with hexagonal 2D lattices.

There are 13 known families of line groups:[25,26] each family includes all groups (with various parameters n, r/q, and partial translation $f = 1/\tilde{q}$) with fixed types of Z group and P factor. The translations of the layer become rotohelical operations T_q^r on the nanotube, giving the first family subgroup 1 $n_p = L^{(1)} = ZP$ ($P = C_q$) of the nanotube line group L (see Table 1). The latter has the same parameters for the ray of the nanotubes $(n_1, n_2) = n(\tilde{n}_1, \tilde{n}_2)$, differing by n.

Apart from the translational invariance, the layer groups have rotational symmetry generated by the rotations around the axis perpendicular to the layer. Table 1 shows that this rotational axis is 6 for graphene monolayer, $\bar{6}$ for BN_{hex} monolayer, and $\bar{3}$ for three-layer titania (fluorite-type) models, respectively. But after the layer rolling only the second-order axis C_2 survives, being compatible with the monoperiodic symmetry. Whenever the order of the principal axis of the layer is 2, 4, or 6, the symmetry of the nanotube is the fifth family line group at least $L^{(5)} = ZP$ ($P = D_n$). As it is seen from Table 1, NTs with general chirality belong to family 5 n_p22 (graphite) or 1 n_p.

In addition, the nonoblique 2D lattices have vertical both mirror and glide planes, but not all of them continue to be symmetry operations for NT. Figure 1 shows three pairs of orthogonal translation vectors for hexagonal lattice: (1,0)-(−1,2), (1,1)-(−1,1), and (0,1)-(−2,1). In each of the three pairs, one translation vector can be chosen as the chiral vector $\tilde{\mathbf{R}}$ and the second as the translation vector. These so-called special chiralities generate the symmetry planes directed along translation vector $\mathbf{L}$ (σ_v) or orthogonal to it (σ_h) and define isogonal point group P_i (Table 1). The symmetry of NTs with the special chiralities is given in ref 26 for all 80 layer groups used for rolling.

2.2. Isomorphism of Line and Plane Groups. The three-dimensional (3D) symmetry transformation matrices $\mathbf{G}^{(3)} = (\mathbf{F}^{(3)}|\mathbf{t}^{(2)})$ corresponding to the layer group of 3D sheet or slab with 2D periodicity, consist of orthogonal $\mathbf{F}^{(3)}$ and translational $\mathbf{t}^{(2)}$ parts. Let the Cartesian axes x, y, and z be directed along the chiral vector $\mathbf{R}$, NT translation vector $\mathbf{L}$, and the layer principal axis perpendicular to the layer, respectively. After the rolling procedure the symmetry operations survive if they do not change the z coordinate (the layer plane is rolled up to cylinder) and, consequently, they must have the form

$$\mathbf{F}^{(3)} = \begin{pmatrix} \mathbf{F}^{(2)} & & 0 \\ & & 0 \\ 0 & 0 & 1 \end{pmatrix} \tag{4}$$

During the transformation described by eq 2 the orthogonal matrices $\mathbf{F}^{(2)}$ undergo the similarity transformation to $\mathbf{F}^{Q}$

$$\mathbf{F}^{Q} = \mathbf{Q}\mathbf{F}^{(2)}\mathbf{Q}^{-1} = \mathbf{P}\tilde{\mathbf{F}}^{Q}\mathbf{P}^{-1} \tag{5}$$

where

$$\tilde{\mathbf{F}}^{Q} = \tilde{\mathbf{Q}}\mathbf{F}^{(2)}\tilde{\mathbf{Q}}^{-1}$$

and

$$\mathbf{P} = \begin{pmatrix} n & 0 \\ 0 & 1 \end{pmatrix}$$

Chirality and translation vectors are supposed to be fixed and $\mathbf{F}^{Q}$ cannot mix or interchange them, so it has to be diagonal (and orthogonal) 2 × 2 matrix

$$\mathbf{F}^{Q} = \tilde{\mathbf{F}}^{Q} = \begin{pmatrix} \pm 1 & 0 \\ 0 & \pm 1 \end{pmatrix} \tag{6}$$

Hence, the orthogonal part of symmetry operations in the basis ($\mathbf{R}$, $\mathbf{L}$) can be represented by one of four of following matrices:

$$\mathbf{E} = \begin{pmatrix} 1 & 0 \\ 0 & 1 \end{pmatrix},\ \mathbf{U} = \begin{pmatrix} -1 & 0 \\ 0 & -1 \end{pmatrix},\ \boldsymbol{\sigma}_{\mathbf{v}} = \begin{pmatrix} -1 & 0 \\ 0 & 1 \end{pmatrix},\ \boldsymbol{\sigma}_{\mathbf{h}} = \begin{pmatrix} 1 & 0 \\ 0 & -1 \end{pmatrix} \tag{7}$$

The transformations (7) include the rotation U by π around the second-order axis, normal to the tube, and reflections in planes, orthogonal to the 2D lattice plane and parallel to the tube axis, directed along translation vector $\mathbf{L}(\sigma_v)$ or orthogonal to it (σ_h). These matrices correspond to orthogonal operations in the first 9 (oblique and rectangular) groups of 17 plane (wallpaper) 2D groups. Moreover, it can be proved that any line group is isomorphic to one of mentioned plane groups when the appropriate periodic boundary conditions are introduced (see below). Due to restricted paper size, we do not give here the proof of this statement. Instead of this we show how this isomorphism appears. Any symmetry operation $\mathbf{G}^{L}$ of line group can be written as combination of 3D orthogonal transformation $\mathbf{F}^{L}$ which mixes only x, y coordinates, and translation along the z ($\mathbf{L}$) direction: $\mathbf{G}^{L} = (\mathbf{F}^{L}|\mathbf{t}^{(1)})$. The upper 2 × 2 submatrix of $\mathbf{F}^{L}$ is also an orthogonal matrix. So, in Cartesian coordinates $\mathbf{G}^{L}$ has the following general form

$$\mathbf{G}^{L} = \begin{pmatrix} \cos\varphi & \sin\varphi & 0 \\ -\delta_1 \sin\varphi & \delta_1 \cos\varphi & 0 \\ 0 & 0 & \delta_2 \end{pmatrix} | (0 \quad 0 \quad \zeta L) \tag{8}$$

where φ (defined by the first-row elements) is allowed rotation angle about the $\mathbf{L}$ axis, $\delta_1,\delta_2 = \pm 1$, and ζ is some fractional or pure translation along $\mathbf{L}$. Introducing the pseudotranslation η by the relation $2\pi\eta = \varphi$ (for which the cyclic boundary condition exists due to period of 2π), one finds correspondence between $\mathbf{G}^{L}$ and the plane (oblique or rectangular) group operation $\mathbf{G}^{(2)}$

$$\mathbf{G}^{(2)} \Leftrightarrow \mathbf{G}^{L};\ \mathbf{G}^{(2)} = \begin{pmatrix} \delta_1 & 0 \\ 0 & \delta_2 \end{pmatrix} | (\eta \quad \zeta) \tag{9}$$

Below we consider this correspondence in more detail for the line group families 4 and 8 describing the symmetry of hexagonal BN and TiO_2 nanotubes.

For the achiral line group families 4 and 8 $\tilde{q} = 2$, $r = 1$, and the generalized translations Z are represented by the screw axis rotations $T_{2n}^{1} = (C_{2n}^{1}|1/2)$ with the helical vector

$$\mathbf{H} = \frac{1}{2n}\mathbf{R} + \frac{1}{2}\mathbf{L} = \frac{1}{2}\tilde{\mathbf{R}} + \frac{1}{2}\mathbf{L}$$

Point factor P consists of E and σ_h or E and σ_v for the families 4 and 8, correspondingly, and also includes pure rotations C_n. Taking into account the eqs 7−9, we can write the corresponding plane group operations in the basis ($\tilde{\mathbf{R}}$, $\mathbf{L}$) as

$$T \Rightarrow \mathbf{E}|(0\ \ 1);\ C_n \Rightarrow \mathbf{E}|(1\ \ 0);\ T_{2n}{}^{1} \Rightarrow \mathbf{E}|(1/2\ \ 1/2); \tag{10}$$

$$\sigma_h \Rightarrow \boldsymbol{\sigma}_\mathbf{h}|(0\ \ 0);\ \sigma_v \Rightarrow \boldsymbol{\sigma}_\mathbf{v}|(0\ \ 0)$$

where $\mathbf{E}$, $\boldsymbol{\sigma}_\mathbf{h}$, and $\boldsymbol{\sigma}_\mathbf{v}$ are the matrices defined in eq 7. It is easy to see that the set of the first line operations together with any one from the second line of eq 10 are the generators of the rectangular centered plane group number 5 (*Cm*) with two different settings, the corresponding layer group is 13 (*Cm*11)). In $\tilde{\mathbf{R}}$ direction the cyclic boundary condition $C_n{}^n \Rightarrow (\mathbf{E}|(1\ 0))^n = \mathbf{E}|(0\ 0)$ must be imposed to provide the isomorphism of plane and line groups. Primitive vectors of this plane lattice can be defined as $\mathbf{a}_1 = \tilde{\mathbf{R}} - \mathbf{H}$ and $\mathbf{a}_2 = \mathbf{H}$

$$\begin{pmatrix}\mathbf{a}_1\\ \mathbf{a}_2\end{pmatrix} = \frac{1}{2}\begin{pmatrix}1 & -1\\ 1 & 1\end{pmatrix}\begin{pmatrix}\tilde{\mathbf{R}}\\ \mathbf{L}\end{pmatrix} \tag{11}$$

2.3. Irreducible Representations of Line Groups: Families 4 and 8. Described isomorphism can be used for obtaining the irreducible representations (IRs) of line groups from the IRs of plane groups. This can be done by projecting of IRs defined in 2D Brillouin zone in reciprocal lattice of corresponding plane group to 1D Brillouin zone of line group. It should be noted, that line group IRs have been already constructed earlier[26,28,29] by the different way for all the families in connection with the stereoregular polymers study.

As example, we consider the construction of IR at X (1/2 1/a) point of Brillouin zone for the line group families 4 and 8. For simplicity we admit that $|\mathbf{R}| = |\mathbf{L}|$. This assumption does not affect the obtained results as IRs of line groups do not depend on $|\mathbf{R}|/|\mathbf{L}|$ ratio. In Figure 2 we show a two-dimensional Brillouin zone for the plane group 5. Reciprocal lattice vectors $\mathbf{b}_L$ and $\mathbf{b}_R$ correspond to ($\tilde{\mathbf{R}}$, $\mathbf{L}$) basis (conventional rectangular centered cell in direct lattice), and vectors $\mathbf{b}_1$ and $\mathbf{b}_2$ to ($\mathbf{a}_1$, $\mathbf{a}_2$) basis (primitive cell). The Brillouin zone for a conventional cell is shown by the dotted lines.

In ($\mathbf{b}_L$, $\mathbf{b}_R$) basis the cyclic boundary conditions for any $\mathbf{k}$ can be written as

$$\exp(2\pi i\mathbf{k}n\tilde{\mathbf{R}}) = \exp(2\pi i n k_R) = 1 \tag{12}$$

where k_R is the component of $\mathbf{k}$ along $\mathbf{b}_R$. The boundary of the first Brillouin zone (for the primitive cell) leads to restriction: $-1 < k_R \leq 1$, and so

$$k_R = \frac{m}{n},\ \ m = 0,\ \pm 1,\ ...,\ \ -n < m \leq n \tag{13}$$

In fact, the 2D Brillouin zone consists of the $2n$ vertical lines parallel to the $\mathbf{b}_L$ axis and crossing the $\mathbf{b}_R$ axis in points with coordinates m/n. All $\mathbf{k}$-points on these lines with the same k_L (or differ by $\mathbf{b}_L$) correspond to line group IR with $k^{(1)} = k_L$.

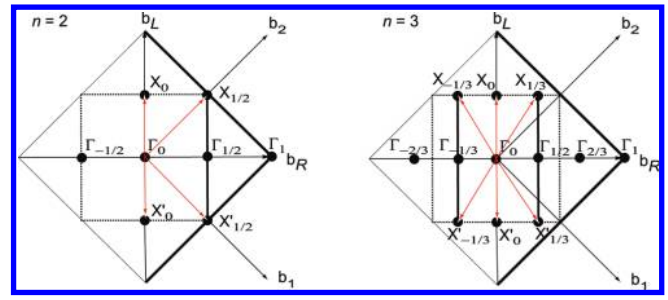

Figure 2. Projection of **k**-points in 2D Brillouin zone for plane group *Cm* to 1D Brillouin zone for line groups of families 4 and 8.

Thus, all points laying on the horizontal lines $k_L = \pm 1/2$ correspond to point X in the first 1D Brillouin zone of the line group. In this case (due to shape of the first 2D Brillouin zone) we have additional restrictions: $-1/2 < k_R \leq 1/2$. It is easy to see that for odd n the point with $\mathbf{k} = (1/2, 1/2)$ does not belong to allowed vertical lines, whereas for even n this point corresponds to $m = n/2$ in eq 13. Taking into account C_s point symmetry of plane group *Cm*, the stars of **k**-vector in 2D Brillouin zone can be generated for each representative of point X. The full IR of plane (and coincidently, line group) can be obtained by inducing from the small IR of the little group of vector $\mathbf{k}$ as it is done for 3D space groups. Because all IRs of point group C_s are one-dimensional, the dimensionality of constructed IR is totally determined by the number of **k**-points in the corresponding star. The stars at point X for the line group of the family 4 are shown in Figure 2 as arrows, and all of them have two rays. The accounting of the time-reversal symmetry may lead to doubling of representation dimensions.

Finally, using the described analysis we found all IRs for line groups of families 4 and 8. For the family 4 at point X there are one 2×2 IR and $(n-1)/2$ 4×4 IRs if n is odd, vs two 2×2 IRs and $(n/2-1)$ 4×4 IRs if n is even. For the family 8 at point X there are two 2×2 IRs and $(n-1)/2$ 4×4 IRs if n is odd, vs three 2×2 IRs and $(n/2-1)$ 4×4 IRs if n is even. The application of this approach to the irreps generation for family 13 (graphene nanotubes with D_{2nh} symmetry) shows that at X point of BZ two 2×2 IRs (odd n) and four 2×2 IRs (even n) appear. The number of 4×4 IRs is the same for family 13 as for families 4 and 8. Our results for IR dimensions agree with those obtained in refs 26, 29, and 30 for family 13. Unfortunately, in ref 31 the dimensions of IRs for achiral CNTs at point X are given incorrectly as the 4×4 IRs are absent in Table 1 of that paper.

3. Computation Details

The first principles LCAO (linear combination of atomic orbitals) calculations on hexagonal BN and titania nanosheets as well as nanotubes have been performed using the hybrid HF-KS (PBE0) exchange-correlation functional.[32] When modeling the hexagonal BN bulk, the all-valence basis sets (BSs) for B and N atoms in the form of 6s-21sp-1d and 6s-31p-1d Gaussian-type functions (GTFs), respectively, have been taken from ref 33. Further BS optimization gave rather negligible changes of the virtual orbitals of BN. Calculated equilibrium lattice constants for the bulk of hexagonal BN structures have been found to be qualitatively close to their experimental values (a_0 of 2.51 Å vs 2.50 Å obtained in experiment and b_0 of 7.0 vs 6.7 Å[17]), thus indicating reliable optimization of BN BSs. On the other hand, unlike the optical band gap energy $\Delta\varepsilon_{gap}$ measured experimentally (5.96 eV for BN_{hex} bulk[34]) the value of $\Delta\varepsilon_{gap}$ calculated by us is found to be noticeably larger (6.94

eV at K point of BZ) which is rather a result of the PBE0 hybrid functional application for BN calculations (since PWGGA functional gave a better agreement of these values[17]).

The small-core pseudopotential[35] of Ti atom is used in titania nanotube calculations (3s, 3p, 3d, and 4s-electrons were taken as valence electrons), while the all-electron BS for O-atom has been taken from ref 36. It is well-known that in the LCAO calculations of crystals the BS of free atom has to be modified as the diffuse functions cause numerical problems because of the large overlap with the core functions of the neighboring atoms in a dense-packed crystal.[37] To optimize the BS in the present study, we use the minimization method without calculations on the total energy derivatives developed by Powell[38] and often called "the method of conjugate directions". The diffuse exponents of valence s, p, and d orbitals have been optimized for stable anatase phase of bulk titania. Its atomic and electronic properties have been reproduced in a good agreement with the experiment (the experimental values are given in parentheses): the lattice parameters $a = 3.784$ Å (3.782 Å) and $c = 9.508$ Å (9.502 Å), the dimensionless parameter for relative position of oxygen atom $u = 0.2074$ (0.2080), although values of $\Delta\varepsilon_{gap}$ are reproduced worse, again being overstimated: 4.0 eV vs 3.2 eV. In any case, these results for the bulk titania (anatase) agree with the experimental data better than those given in ref 39 for both plane wave (PW) and LCAO calculations when using the different exchange-correlation potentials. Certain improvement of substantially underestimated values of $\Delta\varepsilon_{gap}$ for bulk anatase in the DFT PW calculations was achieved recently[23] when using the LDA+U method (2.7 eV).

The monoperiodic translation symmetry has been adopted for our nanotube calculations as it was implemented with POLYMER option in CRYSTAL06 code.[33] Unfortunately, this option takes into account only the symmetry of rod groups being the subset of the nanotube line groups as present in Table 1. A serious attempt to overcome this difficulty has been undertaken recently: the last release of CRYSTAL package[40] contains a special input option which allows generation of 1D nanotubes from 2D slabs. However, the formalism of line groups has not been implemented in CRYSTAL09 code.

4. Structural and Electronic Properties of Hexagonal BN Monolayer and Nanotubes

Description of hexagonal BN bulk and (0001) monolayer, which is similar to the hexagonal structure of graphite bulk and graphene nanosheet, respectively, precedes description of properties for the BN nanotubes, in accordance with a model of structural transformation (3D → 2D → 1D)[19] which means (i) cutting of the monolayer and (ii) its further rolling to a SW NT. Surface energy, E_{surf} (Table 2 and Figure 3) is calculated as

$$E_{surf}(n) = \frac{1}{2S}(E_n - nE_b) \qquad (14)$$

where E_n is the total energy of n-layer slab per primitive surface unit cell and S its area, while E_b is the total energy per primitive bulk unit cell.

The B−N bond population in a semicovalent boron nitride has been found to be 0.575 e for bulk and 0.600 e for the nanosheet (the former has to be smaller, due to the partial interbonding of neighboring (0001) layers in hexagonal BN bulk). The maximum of the electron density within the B−N is localized closer to the midpoint along the semicovalent bond,[41]

TABLE 2: The Structural and Electronic Properties of Optimized BN Hexagonal Bulk and (0001) Nanosheet (Figure 3)

models of BN bulk and sheet	lattice parameters a (Å)	lattice parameters b (Å)	bond length d_{B-N} (Å)	effective charge q_B[a] (e)	E_{surf} (J/m^2)	$\Delta\varepsilon_{gap}$ (eV)
bulk	2.50	6.90	1.445	1.01		6.94
sheet	2.50		1.444	0.99	0.04	7.09

[a] Averaged effective charges q_N are the same as q_B, with opposite sign.

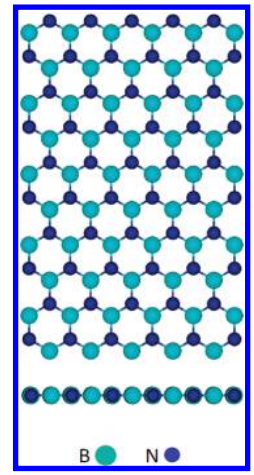

Figure 3. BN(0001) nanosheet: top and across views.

which can be explained by a proximity of ionic radii of the B and N atoms as a result of the electronic charge transfer.

For BN NTs of *ac* and *zz* chiralities (Figure 4) and gradually growing diameters (D_{NT} varies from 0.5 up to 3.3 nm), we analyze a number of different properties (Table 3). For a small D_{NT} (low chirality indices), the absolute values of both relaxation and strain energies are large enough, and trying to reduce these diameters even more, we face their enhanced instability. Since hypothetical nanotubes with infinite diameter should coincide with (0001) monolayer, a consequent growth of the NT diameters leads to a substantial decrease of both relaxation and strain energies (down to zero at infinity), whereas the values of l_{NT}, d_{B-N}, q_B, and $\Delta\varepsilon_{gap}$ (Table 3) approach those for the BN sheet (Table 2). Strain energy is calculated as follows

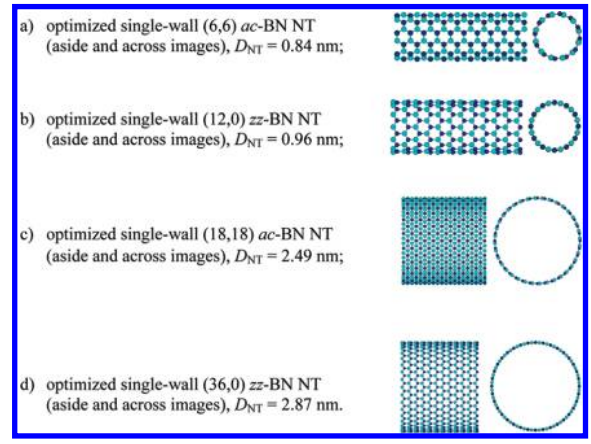

Figure 4. Images of hexagonal SW BN NTs with different chiralities and diameters.

TABLE 3: The Structural and Electronic Properties of Optimized BN Nanotubes (Figure 4)

NT chirality indices	N_a[a]	l_{NT}[b], Å	D_{NT}, Å	d_{B-N}, Å	q_B, e	E_{relax}, eV/BN	E_{strain}, kJ/mol per BN	$\Delta\varepsilon_{gap}$, eV
			(n,n)nanotubes, $C_{2n,h}$ (family 4)					
(4,4)	16	2.505	5.49	1.449	0.990	−0.086	34.69	6.69
(6,6)	24	2.503	8.39	1.447	1.010	−0.035	16.22	6.98
(12,12)	48	2.502	16.61	1.446	1.003	−0.010	5.56	7.01
(18,18)	72	2.502	24.87	1.445	0.997	−0.005	2.14	6.99
(24,24)	96	2.502	33.13	1.445	0.995	−0.004	1.24	7.00
			(n,0) nanotubes, $C_{2n,v}$ (family 8)					
(6,0)	24	4.303	5.01	1.442	0.986	−0.110	46.78	4.96
(12,0)	48	4.328	9.56	1.444	1.012	−0.022	12.44	6.58
(18,0)	72	4.331	14.41	1.444	1.008	−0.010	5.92	7.00
(24,0)	96	4.332	19.12	1.444	1.001	−0.006	2.48	6.98
(36,0)	144	4.333	28.67	1.444	0.994	−0.003	1.62	6.96

[a] N_a, number of atoms per nanotube unit cell. [b] l_{NT}, length of NT unit cell along translation vector.

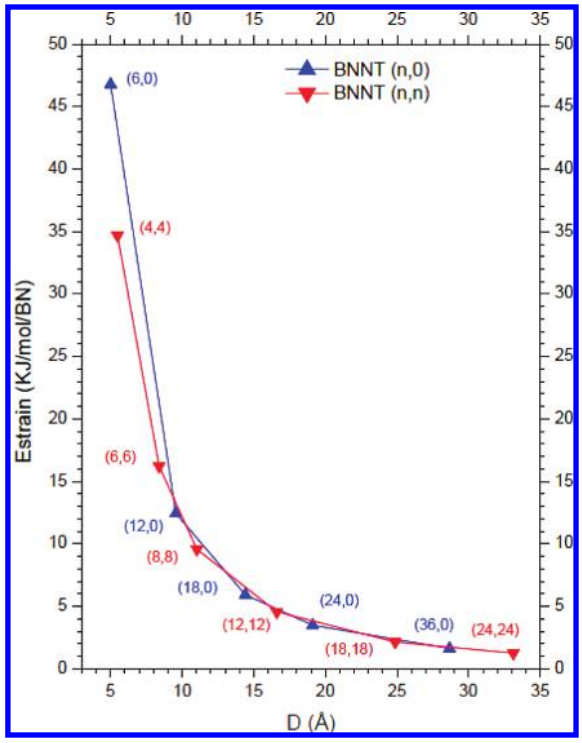

Figure 5. Strain energies E_{strain} vs D_{NT} for the two sets of SW BN NTs with various (n,n) and (n,0) chiralities.

$$E_{strain} = \frac{1}{m}(E_{NT} - kE_{slab}) \qquad (15)$$

being defined via k (number of slab unit cells) containing the same number of BN formula units (m) as in nanotube unit cells, while E_{NT} and E_{slab} are the total energies per corresponding unit cells. E_{relax}, relaxation energy, means a difference between the total energies of nonrelaxed NTs rolled up from the optimized nanosheet and those after relaxation (per BN formula unit).

Energy curves $E_{strain}(D_{NT})$ for BN nanotubes of both chiralities qualitatively coincide (Figure 5), i.e., just NT diameter determines the strain energy. As to $\Delta\varepsilon_{gap}(D_{NT})$ curves (Figure 6), they approach to each other and to the gap of BN sheet for $D_{NT} > 1.5$ nm.

5. Structural and Electronic Properties of Hexagonal TiO_2 Three-Layer Sheets and Nanotubes

TiO_2 sheets with a thickness of a few atomic layers were found to be remarkably stable.[42] Theoretical simulations on TiO_2

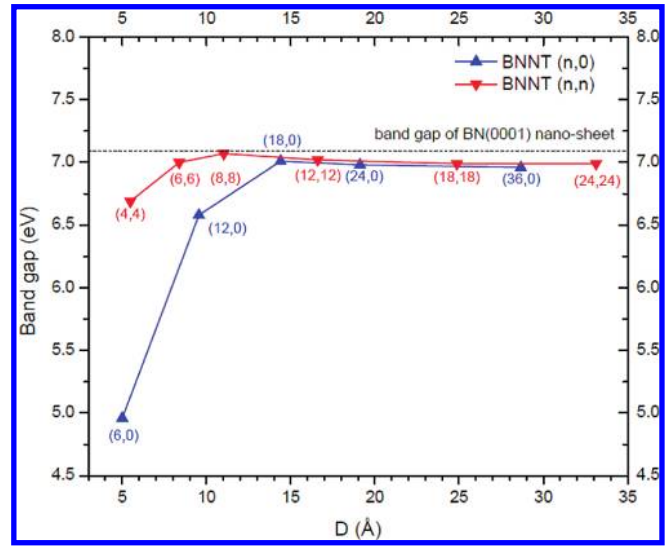

Figure 6. Band gaps $\Delta\varepsilon_{gap}$ vs D_{NT} for the two sets of SW BN nanotubes with various (n,n) and (n,0) chiralities.

nanosheets and nanotubes originating from the three-layer O−Ti−O slabs (Figure 7) were quite widespread so far as more simple systems for simulations.[21] Moreover, when optimizing the structures of three-layer (101) slab cut from anatase bulk we recently obtained just structure of (111) fluorite-type slab[24] which exposes 6-fold coordinated titanium atoms and 3-fold coordinated oxygens (Figure 7a). The main results obtained for this slab compared with the corresponding bulk properties of titania anatase phase are present in Table 4.

Relaxation energy for three-layer TiO_2 slab cut from anatase bulk and transformed to (111) fluorite-type morphology is really large (Table 4) while its surface and formation energies are qualitatively similar to those calculated earlier.[23,42] Since the optimized three-layer slab has a hexagonal structure, its parameters cannot be compared directly with those for titania anatase bulk.

Three-layer titania nanosheets with a hexagonal fluorite-like (111) structure can be rolled up to three-layer titania SW NTs with (i) armchair-type (n,n) chirality and (ii) zigzag-type (n,0) chirality. The optimized structures of the four selected nanotubes of both chiralities (the two nanotube models per each chirality) are shown in Figure 8.

In Table 5, we compare results of calculations on TiO_2 nanotubes shown in Figure 8. As to Ti−O bond lengths, their deformation is more noticeable for smaller values of D_{Ti-O}, gradually approaching to those in three-plane nanosheet (Table

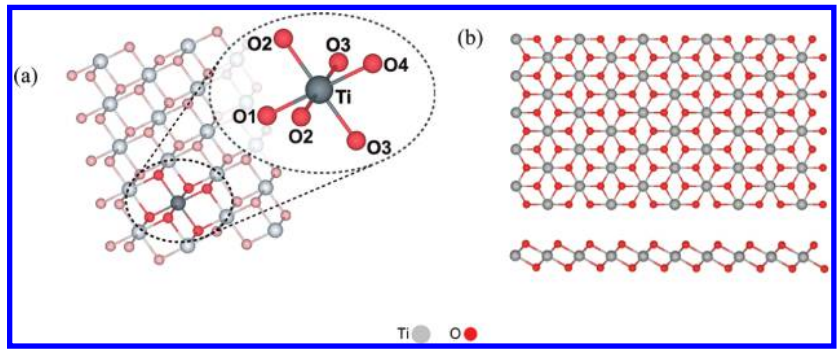

Figure 7. 6-fold coordination of Ti atoms in stoichiometric three-layer hexagonal titania nanosheet (a) as well as its top and across images (b).

TABLE 4: The Atomic and Electronic Structure of Optimized TiO_2 Anatase Bulk vs Fluorite-like (111) Titania Slab

models of TiO_2 bulk and sheets	lattice parameters (Å)		thickness	bond length d_{Ti-O}[a] (Å)				effective charge	E_{relax} per	E_{surf}	
	a	c	h_{NT} (Å)	Ti−O1	Ti−O2	Ti−O3	Ti−O4	q_{Ti}[b] (e)	TiO_2 unit (eV)	(J/m^2)	$\Delta\varepsilon_{gap}$ (eV)
bulk	3.78	9.51		1.935	1.935	1.973	1.973	2.35			4.09
3-layer (fluorite-like)	2.96		1.92	1.95	1.96	1.97	1.98	2.45	−6.05	0.44	4.89

[a] The corresponding bonds are shown in Figure 7a. [b] Averaged effective charges q_O are as twice as small as q_{Ti}, with opposite sign.

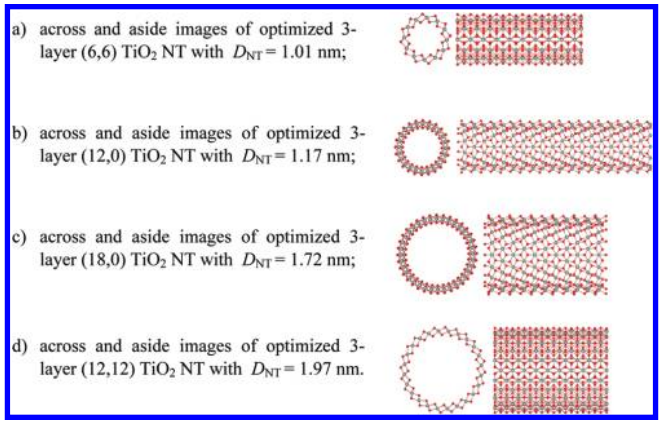

Figure 8. Images of hexagonal SW TiO_2 NTs with different chiralities and diameters.

4). Obviously, this is also true for convergence of E_{relax} with D_{NT} increasing (Table 5).

We also analyze E_{strain} and $\Delta\varepsilon_{gap}$ dependence on D_{NT} for all four sets of three-layer TiO_2 NTs simulated in the present study (Figures 9 and 10, respectively). We consider a large enough range of nanotube diameters, from 0.5 to 4.0 nm, with a number of atoms per NT unit cell increased from 30 up to 288. To construct both plots on Figures 9 and 10, we have performed

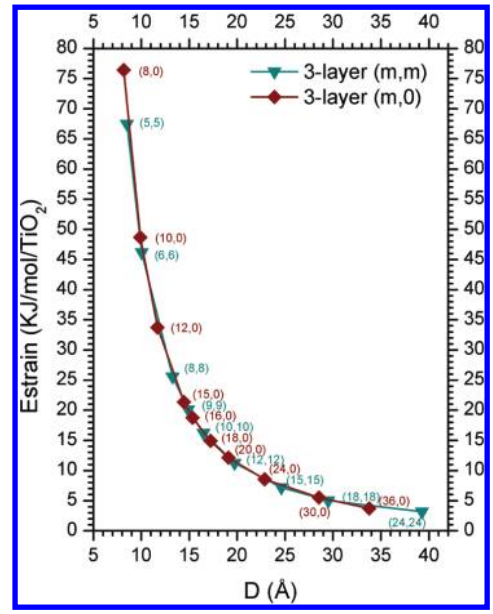

Figure 9. Strain energies E_{strain} vs D_{NT} for the two sets of SW TiO_2 NTs with various chiralities.

calculations with the total geometry optimization for altogether 20 one-periodic models of TiO_2 NTs of different morphologies.

TABLE 5: The Structural and Electronic Properties of Four Hexagonal Three-Layer TiO_2 NTs[a]

chirality of nanotube	N_a	l_{NT} (Å)	D_{NT} (Å)	h_{NT} (Å)	d_{Ti-O} (Å)				q_{Ti} (e)	E_{relax}, per TiO_2 (eV)	E_{strain}, per TiO_2 (kJ/mol)	$\Delta\varepsilon_{gap}$ (eV)
					Ti−O1	Ti−O2	Ti−O3	Ti−O4				
$(2n)_n/m$ group, $C_{2n,h}$ (family 4)												
(6,6)	36	2.991	10.06	1.86	1.89	1.94	2.00	2.05	2.42	−0.09	46.18	4.66
(9,9)	54	2.98	14.88	1.89	1.91	1.94	1.99	2.02	2.43	−0.05	20.11	4.74
(12,12)	72	2.97	19.73	1.91	1.935	1.95	1.98	1.995	2.44	−0.04	11.26	4.77
(15,15)	90	2.97	24.61	1.91	1.94	1.95	1.98	1.99	2.45	−0.04	7.20	4.79
(18,18)	108	2.97	29.51	1.91	1.945	1.955	1.97	1.98	2.45	−0.03	5.04	4.80
$(2n)_nmc$ group, $C_{2n,v}$ (family 8)												
(8,0)	48	5.065	8.17	1.83	1.89	1.94	1.955	2.135	2.40	−0.33	76.43	4.65
(12,0)	72	5.10	11.70	1.88	1.915	1.945	1.96	2.03	2.43	−0.09	33.71	4.70
(18,0)	108	5.12	17.23	1.90	1.935	1.95	1.965	1.965	2.44	−0.05	14.93	4.75
(24,0)	144	5.12	22.88	1.91	1.94	1.95	1.97	1.985	2.45	−0.04	8.55	4.79
(30,0)	180	5.125	28.55	1.92	1.945	1.955	1.975	1.98	2.45	−0.04	5.52	4.82

[a] Definitions of values are the same as in Tables 2−4.

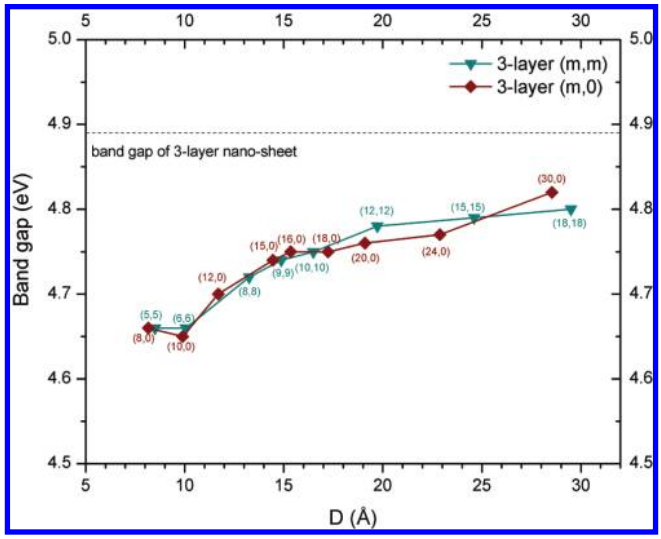

Figure 10. Band gaps $\Delta\varepsilon_{gap}$ vs D_{NT} for the two sets of SW TiO_2 NTs with various chiralities.

Two curves $E_{strain}(D_{NT})$ imaged in Figure 10 for two chiralities of titania nanotubes confirm conclusions drawn above from Table 5. When diameters of nanotubes increase up to 40 Å, all the strain energies substantially decrease and approach each other. We waited to see if further increase of D_{NT} can result in slightly smaller values of E_{strain} for three-layer nanotubes. In the three-layer nanotubes of similar diameters, the difference of the strain energies for fluorite-type (n,n) and $(n,0)$ chiralities is rather negligible, thus supporting qualitatively similar results obtained earlier for these types of nanotubes.[19,21,23] We can also observe qualitative similarity between dependencies of E_{strain} vs D_{NT} shown in Figures 5 and 9 for hexagonal nanotubes of BN and TiO_2, respectively.

Figure 10 presents $\Delta\varepsilon_{gap}(D_{NT})$ curves. When the nanotube diameters markedly increase, their band gaps asymptotically approach those for the corresponding 2D slabs (Table 4), analogously to hexagonal BN NTs (Figure 6). However, the considered nanotube diameters are too small for direct comparison with slabs. In our previous study,[24] we found considerably larger qualitative difference between the pairs of both $E_{strain}(D_{NT})$ and $\Delta\varepsilon_{gap}(D_{NT})$ curves constructed for titania nanotubes of different morphology (i.e., three-layer fluorite-type vs six-layer anatase-type nanotubes).

6. Conclusions

1. Use of the line group formalism allows the construction of nanotubes of different crystalline morphology. The exploitation of the rotohelical symmetry for NTs permits drastic reductions of the computation time. A new approach to the generation of the line group irreducible representations is suggested based on the isomorphism between line and plane groups. The application of the approach suggested for nanotubes is demonstrated for X-point of 1D Brillouin zone and line group families 4 and 8.

2. Ab initio LCAO calculations using the hybrid PBE0 Hamiltonian allow us to perform the analysis of the atomic and electronic structure of BN and TiO_2 sheets as well as nanotubes simulated using different models.

3. The strain energies of SW BN and TiO_2 hexagonal nanotubes are reduced with increasing NT diameter approaching to minimum energy limit beginning with $D_{NT} > 2$ nm while their energy band gaps approach to those for the corresponding 2D slabs. However, the values D_{NT} are too small to compare the calculated nanotube properties with those for the corresponding slabs.

4. Comparison of $E_{strain}(D_{NT})$ and $\varepsilon_{gap}(D_{NT})$ curves for SW BN and NTs of different crystalline morphology shows quite expected qualitative similarities for properties of hexagonal nanotubes (BN and fluorite-type TiO_2) regardless of their chemical difference.

Acknowledgment. R.E. is grateful to Professor M. Damnjanović for stimulating discussions, S.P. is thankful for the financial support through the ESF Project No. 2009/0216/1DP/1.1.1.2.0/09/APIA/VIAA/044. The authors thank M. V. Losev for essential contribution in development of computational formalism used in this study.

References and Notes

(1) Haubner, R.; Wilhelm, M.; Weissenbacher, R.; Lux, B. In *High Performance Non-oxide Ceramics II*; Structure and Bonding 102; Springer: Berlin, Heidelberg, New York, 2002; pp 1−45.
(2) Muscat, J.; Swamy, V.; Harrison, N. M. *Phys. Rev. B* **2002**, *65*, 224112.
(3) Chopra, N. G.; Luyken, R. J.; Cherrey, K.; Crespi, V. H.; Cohen, M. L.; Louie, S. G.; Zettl, A. *Science* **1995**, *269*, 966–967.
(4) Golberg, D.; Bando, Y.; Eremets, M.; Takemura, K.; Kurashima, K.; Yusa, H. *Appl. Phys. Lett.* **1996**, *69*, 2045–2047.
(5) Loiseau, A.; Willaime, F.; Demoncy, N.; Hug, G.; Pascard, H. *Phys. Rev. Lett.* **1996**, *76*, 437–440.
(6) Bengu, E.; Marks, L. D. *Phys. Rev. Lett.* **2001**, *86*, 2385–2389.
(7) Czerw, R.; Webster, S.; Carroll, D. L.; Vieira, S. M. C.; Birkett, P. R.; Rego, C. A.; Roth, S. *Appl. Phys. Lett.* **2003**, *83*, 1617–1619.
(8) Wang, W.; Varghese, O. K.; Paulose, M.; Grimes, C. A. *J. Mater. Res.* **2004**, *19*, 417–422.
(9) Zhao, J.; Wang, X.; Sun, T.; Li, L. *Nanotechnology* **2005**, *16*, 2450–2454.
(10) Viriya-empikul, N.; Sano, N.; Charinpanitkul, T.; Kikuchi, T.; Tanthapanichakoon, W. *Nanotechnology* **2008**, *19*, 035601.
(11) Tenne, R.; Seifert, G. *Annu. Rev. Mater. Res.* **2009**, *39*, 387–413.
(12) Mowbray, D. J.; Martinez, J. I.; Garcýa Lastra, J. M.; Thygesen, K. S.; Jacobsen, K. W. *J. Phys. Chem. C* **2009**, *113*, 12301–12308.
(13) Blase, X.; Rubio, A.; Louie, S. G.; Cohen, M. L. *Europhys. Lett.* **1994**, *28*, 335–340.
(14) Miyamoto, Y.; Rubio, A.; Berber, S.; Yoon, M.; Tománek, D. *Phys. Rev. B* **2004**, *69*, 121413.
(15) Piquini, P.; Baierle, R. J.; Schmidt, T. M.; Fazzio, A. *Nanotechnology* **2005**, *16*, 827–831.
(16) Zobelli, A.; Ewels, C. P.; Gloter, A.; Seifert, G.; Stephan, O.; Csillag, S.; Colliex, C. *Nano Lett.* **2006**, *6*, 1955–1960.
(17) Zhukovskii, Yu. F.; Piskunov, S.; Pugno, N.; Berzina, B.; Trinkler, L.; Bellucci, S. *J. Phys. Chem. Solids* **2009**, *70*, 796–803.
(18) Wang, Y. Q.; Hu, C. G.; Duan, X. F.; Sun, H. L.; Hue, Q. K. *Chem. Phys. Lett.* **2002**, *365*, 427–431.
(19) Enyashin, A. N.; Seifert, G. *Phys. Status Solidi B* **2005**, *242*, 1361–1370.
(20) Liu, Z.; Zhang, Q.; Qin, L. C. *Solid State Commun.* **2007**, *141*, 168–171.
(21) Wang, J.; Wang, L.; Ma, L.; Zhao, J.; Wang, B.; Wang, G. *Physica E* **2009**, *41*, 838–842.
(22) Bandura, A. V.; Evarestov, R. A. *Surf. Sci.* **2009**, *603*, L117–L120.
(23) He, T.; Zhao, M.; Zhang, X.; Zhang, H.; Wang, Z.; Xi, Z.; Liu, X.; Yan, S.; Xia, Y.; Mei, L. *J. Phys. Chem. C* **2009**, *113*, 13610–13615.
(24) Evarestov, R. A.; Bandura, A. V.; Losev, M. V.; Piskunov, S.; Zhukovskii, Yu. F. *Physica E*, in press.
(25) Vujicic, M.; Bozovic, I. B.; Herbut, F. *J. Phys. A: Math. Gen.* **1977**, *10*, 1271–1279.
(26) Damnjanovic, M.; Miloševic, I. *Line Groups in Physics: Theory and Applications to Nanotubes and Polymers*; Lecture Notes in Physics, 801; Springer: Heidelberg and New York, 2010.
(27) *International Tables for Crystallography, volume E, Subperiodic Groups*; Kopsky, V., Litvin, D. B., Eds.; Kluwer Academic Publishers: Dodrecht/Boston/London, 2002.
(28) Vujicic, M.; Bozovic, I. B.; Herbut, F. *J. Phys. A: Math. Gen.* **1978**, *11*, 2133–2147.
(29) Bozovic, I. B.; Vujicic, M. *J. Phys. A: Math. Gen.* **1981**, *14*, 777–795.
(30) Tobin, M. C. *J. Mol. Spectrosc.* **1960**, *4*, 349–358.
(31) Barros, E. B.; Jorio, A.; Samsonidze, G. G.; Capaz, R. B.; Filho, A. G. S.; Dresselhaus, G.; Dresselhaus, M. S. *Phys. Rep.* **2006**, *431*, 261–302.
(32) Adamo, C.; Barone, V. *J. Chem. Phys.* **1999**, *110*, 6158–6170. Ernzerhof, M.; Scuseria, G. E. *J. Chem. Phys.* **1999**, *110*, 5029–5036.

(33) Dovesi, R.; Saunders, V. R.; Roetti, C.; Orlando, R.; Zicovich-Wilson, C. M.; Pascale, F.; Civalleri, B.; Doll, K.; Harrison, N. M.; Bush, I. J.; D'Arco, Ph.; Llunell, M. *CRYSTAL-2006 User Manual*; University of Turin: Turin, 2006.

(34) Evans, D. A.; McGlynn, A. G.; Towlson, B. M.; Gunn, M.; Jones, D.; Jenkins, T. E.; Winter, R.; Poolton, N. R. J. *J. Phys.: Condens. Matter* **2008**, *20*, 075233.

(35) Hurley, M. M.; Pacios, L. F.; Christiansen, P. A.; Ross, R. B.; Ermler, W. C. *J. Chem. Phys.* **1986**, *84*, 6840–6853.

(36) Schäfer, A.; Huber, C.; Ahlrichs, R. *J. Chem. Phys.* **1994**, *100*, 5829–5835.

(37) Evarestov, R. A. *Quantum Chemistry of Solids. The LCAO First Principles Treatment of Crystals*; Springer Series in Solid State Sciences, 153; Springer Verlag: Berlin, 2007.

(38) Press, W. H.; Teukolski, S. A.; Vetterling, V. T.; Flannery, B. P. *Numerical Recipes in FORTRAN 77: The Art of Scientific Computing*, 3rd ed.; Cambridge University Press: Cambridge, 2007; Vol. 1.

(39) Labat, F.; Baranek, P.; Domain, C.; Minot, C.; Adamo, C. *J. Chem. Phys.* **2007**, *126*, 154703–154713.

(40) Dovesi, R.; Saunders, V. R.; Roetti, C.; Orlando, R.; Zicovich-Wilson, C. M.; Pascale, F.; Civalleri, B.; Doll, K.; Harrison, N. M.; Bush, I. J.; D'Arco, Ph.; Llunell, M. *CRYSTAL-2009 User Manual*; University of Turin: Turin, 2010.

(41) Lichanot, A.; Azavant, P.; Pietsch, U. *Acta Crystallogr., Sect. B* **1996**, *52*, 586–595.

(42) Vittadini, A.; Casarin, M. *Theor. Chem. Acc.* **2008**, *120*, 551–556.

JP106929F